Materials Advances

ROYAL SOCIETY OF CHEMISTRY

PAPER

View Article Online
View Journal | View Issue

Cite this: *Mater. Adv.*, 2023, 4, 2308

Schiff bases as analytical tools: synthesis, chemo-sensor, and computational studies of 2-aminophenol Schiff bases†

Felicia Ndidi Ejiah, * Mujeeb Olarewaju Rofiu, Oluwakemi Adekunbi Oloba-Whenu and Tolulope Mojisola Fasina

Received 1st March 2023,
Accepted 5th April 2023

DOI: 10.1039/d3ma00097d

rsc.li/materials-advances

Schiff bases of 2-((2-hydroxybenzylidene)amino)phenol (**MJ$_1$**) and 4-bromo-2-(((2-hydroxyphenyl)-imino)methyl)phenol (**MJ$_2$**) were synthesized from 2-aminophenol and screened for the detection of some biologically important metal ions. UV-vis spectroscopy screening, electrochemical studies, and theoretical calculations of the ligands (**MJ$_1$** and **MJ$_2$**) revealed the sensing properties of the probes. The binding interactions of probes **MJ$_1$** and **MJ$_2$** with Cu^{2+}, Zn^{2+}, and Ni^{2+} resulted in redshifts in the absorption maxima. **MJ$_1$** exhibited reversibility of its metal complexes with Cu^{2+} and Zn^{2+} in an EDTA solution. The electrochemical behavior of both probes with Cu^{2+}, Zn^{2+}, Ni^{2+}, Cr^{3+} resembled voltammograms with one or two quasi-reversible redox processes, indicating complex formation between the probes and metal ions. The electrochemical screening showed none or insignificant binding interactions between the probes with Cr^{3+}. The change in electro-activeness of ligands **MJ$_1$** and **MJ$_2$** upon complexation with metal ions (Cu^{2+}, Zn^{2+}, and Ni^{2+}) suggested a metal-to-ligand charge transfer (MLCT) and intramolecular charge transfer binding mechanism. The complex formed between the sensor and ligand was determined using density functional theory employing the B3LYP functional and the LANL2DZ and 6-311+G(d,p) basis sets. Atomic charge and molecular orbital analyses of the frontier molecular orbitals also support the MLCT mechanism. The global reactivity descriptor parameters show that **MJ$_2$** may be a better electron acceptor than **MJ$_1$**.

Introduction

The development of chemo-sensors has attracted increasing interest in the scientific world in recent years due to interdisciplinary applications across chemistry, chemical engineering, biology, biochemistry, medicine, and environmental sciences.[1–3] Chemo-sensors are molecules that can detect changes in one or more physicochemical properties.[4,5] The simplicity, low detection limits, high selectivity and sensitivity, cost-effectiveness, real-time monitoring with short response time, and versatility in most chemo-sensor design and applications contribute to the special attention in this area of research.[6–9] The vital role of metal ions in biological systems comes from the uncontrolled amount of these ions and their recommended amount in food, water, and biological fluids. Special need for simple and highly effective analytical methods for probing and monitoring biologically and environmentally essential transition metal ions is imminent.[6] Previous methods demand well-trained personnel, high-cost and sophisticated analytical instruments, and time-consuming sample preparation processes.[10–19]

Among the biologically and environmentally essential transition metals ions, zinc is the second-most abundant metal in the brain.[20] A zinc ion is a divalent cation that helps in regulating intracellular signal transduction and gene expression through transcription factor activity.[21] About 10% of the total Zn(II) in the brain is co-located and co-released from synaptic vesicles with glutamate, and therefore, it plays a vital role as a metal neurotransmitter by regulating the synaptic and neuronal activity.[22] Zinc ions have been linked to neurological diseases such as Parkinson's disease and Alzheimer's disease. Extracellular Zn(II) concentrations have been displayed in epilepsy and can also lead to excitotoxicity.[23]

The use of mass spectrometry to detect Zn(II) in the brain prohibits the dynamic tracking of extracellular signaling.[24] Further, on rapid timescales, fluorescence imaging in the detection of Zn^{2+} poses a difficulty in the quantitative determination of concentration levels.[25] Recently, an electrochemical technique called fast-scan cyclic voltammetry at carbon-fiber microelectrodes (FSCV-CFM) has enabled the rapid detection of electroactive neurochemicals in tissue.[26]

Department of Chemistry, University of Lagos, Akoka, Lagos, Nigeria.
E-mail: fejiah@unilag.edu.ng

† Electronic supplementary information (ESI) available. See DOI: https://doi.org/10.1039/d3ma00097d

An important metal with the foremost role in the nervous system is copper. It functions as a co-factor of many metalloenzymes by taking an active part, including superoxide dismutase, cytochrome *c* oxidase, and tyrosinase.[27] Its occurrence along with its distinct use as a thermo-electric material makes it very crucial for use in different industries.[28] Copper also functions in the regulation of metabolism, build-up of connective tissues by fixing calcium in bones, as well as having antifungal and antiyeast characteristics. It plays an important role in maintaining estrogen metabolism and the production of cellular energy.[29] Due to the antimicrobial potency of most copper compounds, copper is used as an active ingredient in many drugs, particularly during copper deficiency.[30] However, unregulated or disrupted copper-ion homeostasis is related to many neurogenerative diseases such as Menkes, Alzheimer's, Wilson's, amyotrophic lateral sclerosis, and Parkinson's diseases.[31] Excessive loading of copper may also be potentially toxic with various body deregulations.[32]

Nickel is another essential trace element in biological systems and is involved in respiration, biosynthesis, and metabolism.[33,34] Nickel actively functions in various enzymatic activities such as acetyl co-enzyme, catalytic processes, superoxide dismutase, carbon monoxide dehydrogenases, and acireductone dioxygenases.[35,36] Loss or deficiency of nickel homoeostasis is harmful to prokaryotic and eukaryotic organisms.[37] Excessive exposure of the body system to nickel can lead to asthma, respiratory system cancer, cardiovascular diseases, nasopharyngeal carcinoma, kidney diseases, and other serious central nervous system disorders.[38] Considering the importance of these metal ions in the body, there arises a need for the rational design of efficient sensors to detect Zn^{2+}, Cu^{2+}, and Ni^{2+} at environmental and biological levels. Some physicochemical properties such as color, fluorescence, or redox potentials upon host–guest interactions have established the use of some molecules as a chemo-sensor.[39]

A variety of sensing mechanisms have been reported for chemo-sensors designed for Cu^{2+}, Zn^{2+}, and Ni^{2+}.[40–44] There have been reports of Schiff bases of 2-aminophenols as chemo-sensors due to their ability to coordinate to some metal ions in solutions,[45–49] but none of them have been used in the evaluation of 2-aminophenol with salicylaldehyde **MJ$_1$** and 5-bromosalicylaldehyde **MJ$_2$** as a chemo-sensor in the detection of Cu^{2+} and Zn^{2+} in solution.

Based on this, our aim is to synthesize and characterize 2-aminophenol Schiff bases as chemo-sensors for Cu^{2+}, Zn^{2+}, and Ni^{2+} in aqueous solutions. We also report a density functional theory (DFT) study of the copper complexes obtained and the mechanism of interaction between the ligands and metal ions.

Results and discussion

Synthesis and characterization of Schiff-base chemo-sensors

The general synthesis scheme for **MJ$_1$** and **MJ$_2$** is provided in Scheme 1.

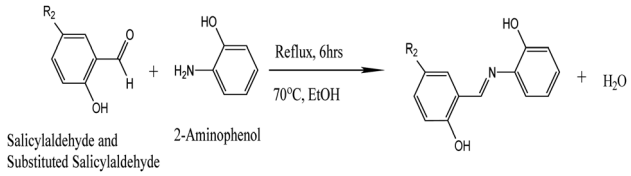

Scheme 1 General synthesis scheme for **MJ$_1$** and **MJ$_2$** **MJ$_1$** = R_2, H; **MJ$_2$** = R_2, Br.

Table 1 IR band (cm^{-1}) of Schiff bases

Compound	R_1	R_2	ν(O–H)	ν(C═N)	ν(C–O)
MJ$_1$	H	H	3173	1630	1275 1222
MJ$_2$	H	Br	3028	1628	1270 1219

FTIR, ESI-MS, and ^{1}H NMR spectra of MJ$_1$ and MJ$_2$

The IR spectra of Schiff bases **MJ$_1$** and **MJ$_2$** (summarized in Table 1) show bands in the regions expected for the ligands. Both compounds displayed bands at 1630–1629 cm^{-1}, 3052–3431 cm^{-1}, and 1275–1219 cm^{-1}, characteristic of the imine C═N, –OH and C–O groups, respectively. The absence of a band at 1720–1740 cm^{-1} due to C═O carbonyl indicates the formation of a Schiff base (Fig. 1 and 2).

ESI-MS spectra confirmed the exact mass of ligands **MJ$_1$** $C_{13}H_{11}NO_2$ $[M + 1H]^{+1}$ m/z = 214.08, found 214.09 and **MJ$_2$** $C_{13}H_{10}BrNO_2$ $[M - 1H]^{-1}$ m/z = 289.99, found 289.98, whereas the ^{1}H NMR spectra revealed resonated protons at the expected values, confirming the purity and structure of **MJ$_1$** and **MJ$_2$** ligands (Fig. 3–6).

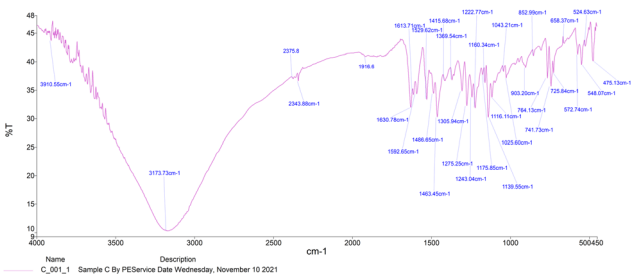

Fig. 1 IR spectra of Schiff base **MJ$_1$**.

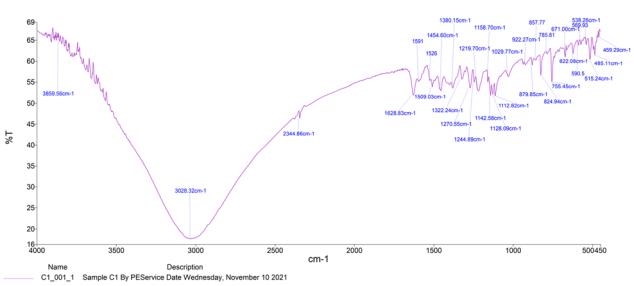

Fig. 2 IR spectra of Schiff base **MJ$_2$**.

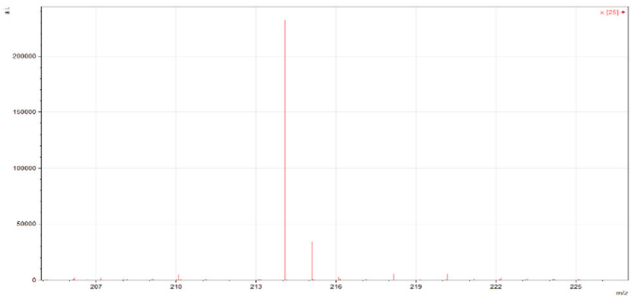

Fig. 3 ESI-MS spectra of $\mathbf{MJ_1}$ $[M + 1H]^{+1}$ m/z = 214.09.

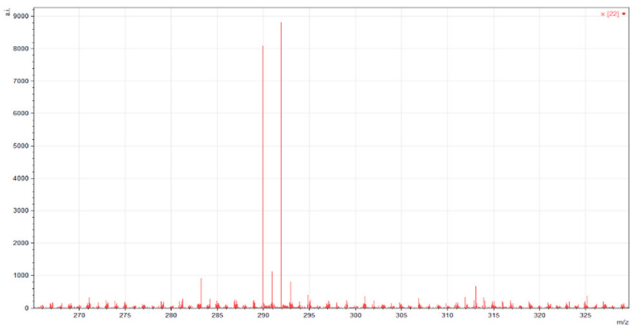

Fig. 4 ESI-MS spectra of $\mathbf{MJ_2}$ $[M - 1H]^{-1}$ m/z = 289.98.

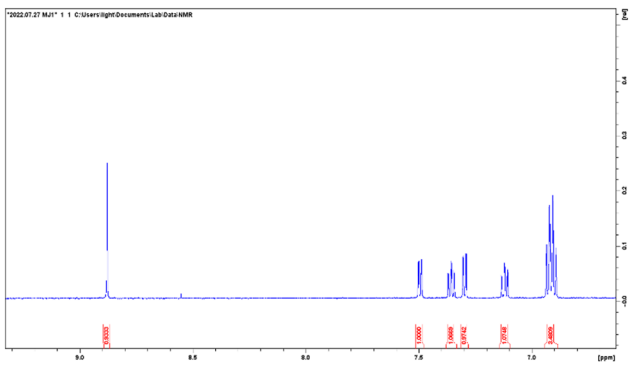

Fig. 5 ^{1}H NMR spectra of $\mathbf{MJ_1}$.

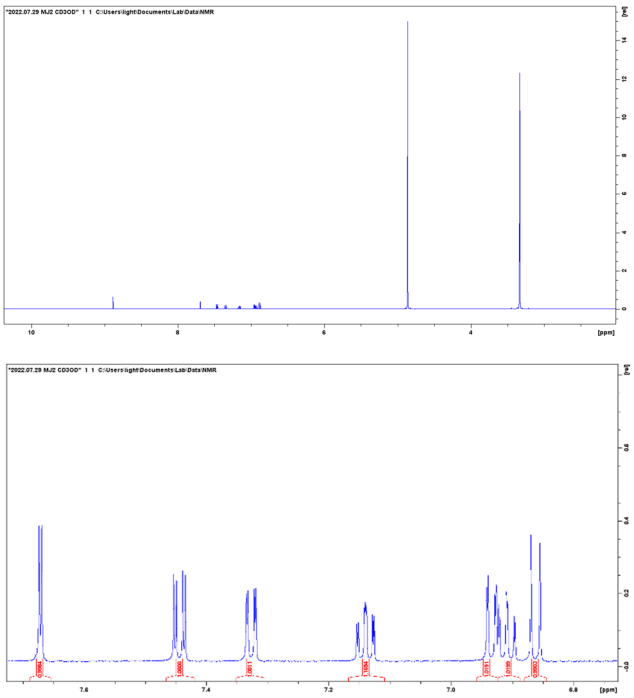

Fig. 6 ^{1}H NMR spectra of $\mathbf{MJ_2}$.

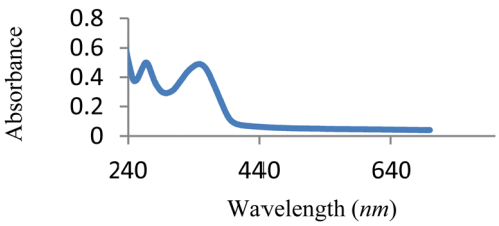

Fig. 7 UV-vis spectra of free $\mathbf{MJ_1}$.

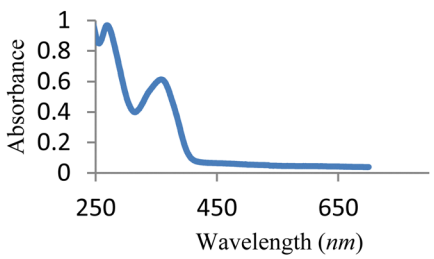

Fig. 8 UV spectra of free $\mathbf{MJ_2}$.

Absorption spectroscopy

The UV-vis spectrum of free $\mathbf{MJ_1}$ and $\mathbf{MJ_2}$ are shown in Fig. 7 and 8. Both Schiff bases displayed a high-energy absorption band in the UV region, namely, 271–274 nm and 352–363 nm. The first band could be attributed to the $\pi \rightarrow \pi^*$ transition of the aromatic ring, while the second band is assigned to the $n \rightarrow \pi^*$ transition of the imine group of the Schiff base moiety.

UV-vis titration studies

The absorption wavelength was observed at 352 nm for $\mathbf{MJ_1}$. Upon the addition of Cu^{2+}, Zn^{2+}, and Ni^{2+}, redshifts were observed for $\mathbf{MJ_1}$ from 352 nm to 415 nm, 426 nm, and 435 nm, respectively. These redshifts depict the association of sensor $\mathbf{MJ_1}$ with Cu^{2+}, Zn^{2+}, and Ni^{2+}, as shown in Fig. 9a. Further, the absorption wavelength at 271 nm for the receptor exhibited different responses upon the addition of metals. A redshift at 271 nm was observed upon the addition of Cu^{2+} and Zn^{2+} at low concentrations followed by the disappearance of the new redshift band on increase in the concentration of Cu^{2+} and Zn^{2+}, as depicted in Fig. 9b and c. This suggests ligand-to-metal charge transfer (LMCT) from the imine group to the metal ion. Further, on the addition of Ni^{2+} (Fig. 9d), the band at 271 nm displayed a bathochromic shift (redshift) and an increase in intensity at 294 nm with an increase in

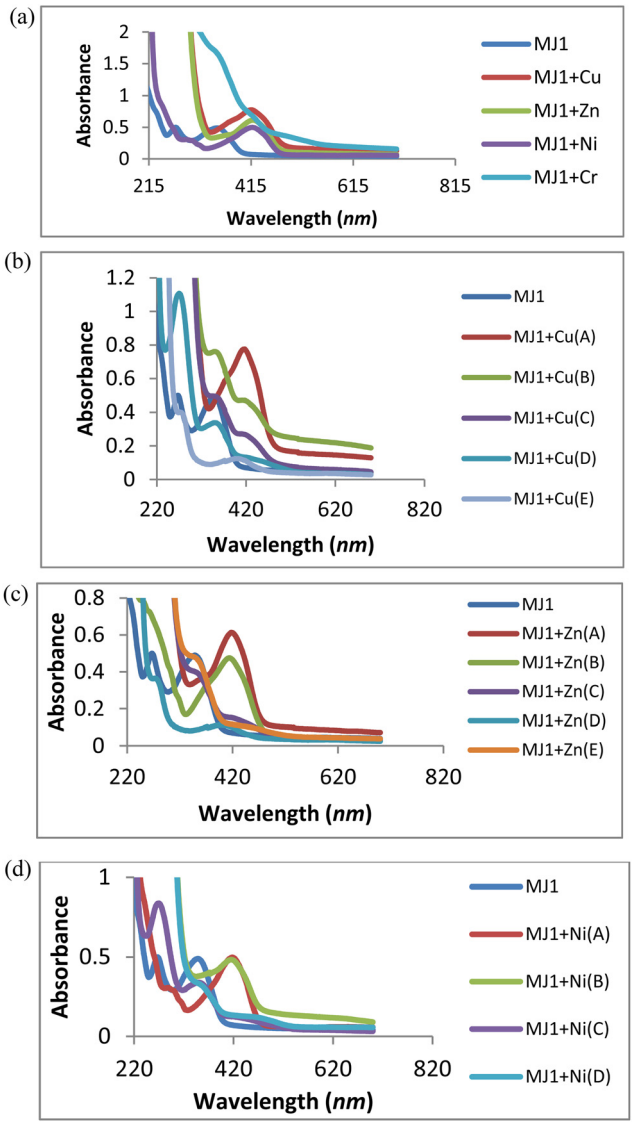

Fig. 9 (a) Titration experiment of $\mathbf{MJ_1}$ (20 μM) with Cu^{2+}, Zn^{2+}, Ni^{2+}, and Cr^{3+}. (b) UV titration of $\mathbf{MJ_1}$ with Cu^{2+} at various concentrations (*A* = 2.5 mM, *B* = 0.625 mM, *C* = 0.156 mM, *D* = 0.039 mM, *E* = 0.00975 mM). (c) UV titration of $\mathbf{MJ_1}$ with Zn^{2+} at various concentrations (*A* = 2.5 mM, *B* = 0.625 mM, *C* = 0.156 mM, *D* = 0.039 mM, *E* = 0.00975 mM). (d) UV titration of $\mathbf{MJ_1}$ with Ni^{2+} at various concentrations (*A* = 2.5 mM, *B* = 0.625 mM, *C* = 0.156 mM, *D* = 0.039 mM).

concentration. This may imply the contribution of the imine group to the association of receptor $\mathbf{MJ_1}$ with Ni^{2+}. This dissimilar observations of Cu^{2+}, Zn^{2+}, and Ni^{2+} with $\mathbf{MJ_1}$ at 271 nm may also be due to their Lewis acid nature and chelation effect. On the basis of this binding mode on addition of a metal ion, the bathochromic shift in the absorption spectra can be explained by intramolecular charge transfer (ICT). Here, Cu^{2+}, being a paramagnetic metal, is highly unstable and more reactive probably due to its d^9 system. Therefore, Zn^{2+} exhibits stronger Lewis acidic nature than Cu^{2+}, which explains the increased tendency of Zn^{2+} to be involved in chelation with a ligand/probe than Cu^{2+}. Similarly, Ni^{2+} exhibits a weaker Lewis acidic nature and is more unstable than Zn^{2+}, and it chelates less readily compared with Zn^{2+} with sensor $\mathbf{MJ_1}$ through both imine and phenolic groups on the receptor.

The association of a metallic ion to the oxygen atom of the phenolic group and nitrogen atom of the Schiff base moiety (C═N) increases its electron-withdrawing feature, leading to a stronger ICT from the electron-donating hydroxyl group to the metal complex. Furthermore, the absorption bands of receptor–metal for $\mathbf{MJ_1}$–Cu^{2+}, $\mathbf{MJ_1}$–Zn^{2+}, and $\mathbf{MJ_1}$–Ni^{2+} complexes shifted to a higher intensity in the spectra of the new complexes, indicating the involvement of the phenolic group in coordination with the central metal atom. In addition, the interaction of the donor site of chemo-sensor ligand $\mathbf{MJ_1}$ rapidly chelates to Cu^{2+}, Zn^{2+}, and Ni^{2+}. Due to this rapid formation of chelation with ligand $\mathbf{MJ_1}$, the respective absorption bands at 415, 426, and 435 nm underwent a decrease in their intensity and total disappearance in $\mathbf{MJ_1}$–Cu^{2+} and $\mathbf{MJ_1}$–Zn^{2+} complexes as the concentrations are reduced. Chelate formation may be due to ICT and LMCT.[50–53]

Moreover, the spectra shown in Fig. 9a exhibits poor or no binding interaction on the addition of Cr^{3+} to sensor $\mathbf{MJ_1}$ as there appears to be no band shift or the appearance of a new band.

A similar trend of interaction was observed for $\mathbf{MJ_2}$ (Fig. 10a–d). The absorption band at 363 nm shifted to 434, 440, and 438 nm upon the addition of Cu^{2+}, Zn^{2+}, and Ni^{2+}, respectively, confirming complex formation. These redshifts depict the association of sensor $\mathbf{MJ_2}$ with Cu^{2+}, Zn^{2+}, and Ni^{2+}. Further, the absorption wavelength at 274 nm for the receptor exhibited different responses upon the addition of metals. On addition of Cu^{2+} and Zn^{2+}, the band at 274 nm displayed a bathochromic shift with an increase in intensity of the new band as the concentration of metal ions increased (Fig. 10b and c). This may imply a contribution of the imine group to the association of receptor MJ_2 with Cu^{2+} and Zn^{2+}. Furthermore, the interaction of Ni^{2+} with $\mathbf{MJ_2}$ exhibited an immediate disappearance of the band at 274 nm and appearance of a new band at 431 nm with an increase in the absorption intensity upon an increase in concentration (Fig. 10d). This also suggests LMCT of the imine group in complexation. As discussed in the interaction of the metal ions with ligand $\mathbf{MJ_1}$, these similar observations of Cu^{2+}, Zn^{2+}, and Ni^{2+} with $\mathbf{MJ_2}$ at 274 nm may also be due to their Lewis acid nature and chelation effect.

Furthermore, the absorption bands of receptor–metal for $\mathbf{MJ_2}$–Cu^{2+}, $\mathbf{MJ_2}$–Zn^{2+}, and $\mathbf{MJ_2}$–Ni^{2+} complexes shifted to low intensity in the spectra of the new complexes, indicating the involvement of phenolic and imine groups in coordination with the central metal atom. As described in the chelation with ligand $\mathbf{MJ_1}$, the respective bathochromic shift in the absorption band at 363 nm ascribed to the n → π* transition in the imine group of the Schiff base moiety to 434, 440, and 438 nm in the formation of complexes results in the low intensity of the free-ligand band at 363 nm as the metallic-ion concentration increases, as revealed by the spectra. This response can also be attributed to ICT and LMCT.

Limit of detection of MJ_1 and MJ_2 probes

The response on addition of the varied concentrations of metal ions ranging from 2.5 mM to 9.77 μM (A–E) with a dilution

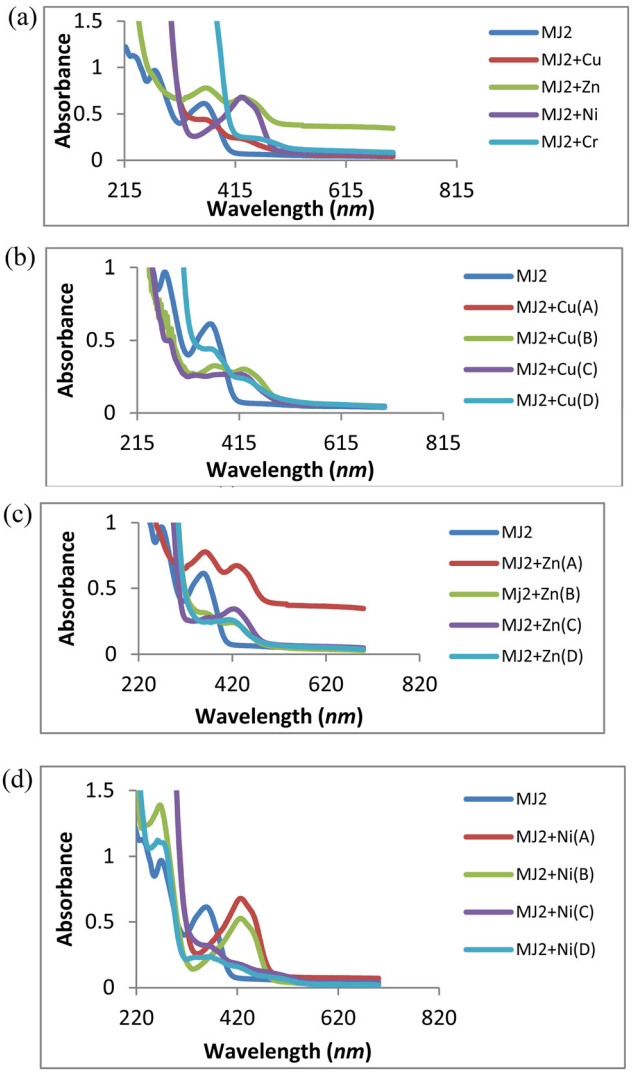

Fig. 10 (a) Titration experiment of **MJ_2** (20 μM) with Cu^{2+}, Zn^{2+}, Ni^{2+}, and Cr^{3+}. (b) UV titration of **MJ_2** with Cu^{2+} at various concentrations (*A* = 2.5 mM, *B* = 0.625 mM, *C* = 0.156 mM, *D* = 0.039 mM). (c) UV titration of **MJ_2** with Zn^{2+} at various concentrations (*A* = 2.5 mM, *B* = 0.625 mM, *C* = 0.156 mM, *D* = 0.039 mM). (d) UV titration of **MJ_2** with Ni^{2+} at various concentrations (*A* = 2.5 mM, *B* = 0.625 mM, *C* = 0.156 mM, *D* = 0.039 mM).

factor of 4 to both sensors **MJ_1** and **MJ_2** suggested the possible limit of detection of the ligands. This indicates sensing at a concentration below the recommended Cu^{2+}, Zn^{2+}, and Ni^{2+} limits in drinking water and the environment. The World Health Organization (WHO) or Environmental Protection Agency (EPA) recommended the maximum acceptable concentration (MAC) of copper, zinc, and nickel in drinking water as 1.5, 3.0, and 0.1 mg L^{-1}, respectively.[54,55]

Reversibility studies of MJ_1 and MJ_2

A reversibility study of the ligands is depicted in Schemes 2 and 3. The UV spectra (Fig. 11a–f) represent the reversibility of ligands **MJ_1** and **MJ_2** using 0.01 M EDTA solution. The spectra show the disappearance of bathochromic-shift bands after complex formation and the resurfacing of n → π* and

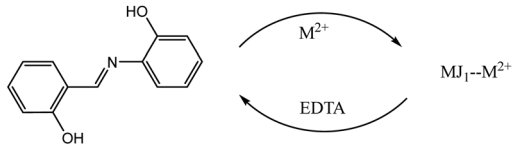

(Z)-2-((2-hydroxybenzylidene)amino)phenol
(MJ_1)

Scheme 2 Reversibility studies of **MJ_1**.

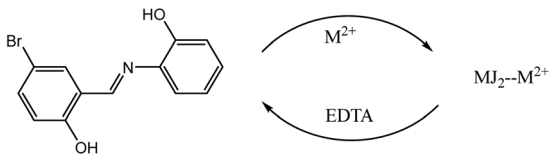

(Z)-4-bromo-2-(((2-hydroxyphenyl)imino)methyl)phenol
(MJ_2)

Scheme 3 Reversibility studies of **MJ_2**.

π → π* transitions of the free ligands. The ligands with varied concentrations of metals were selected and spiked with 0.01 M EDTA solutions and all of them proved to be reversible.

Electrochemical studies

Electrochemical behavior of MJ_1 with Cu^{2+}, Zn^{2+}, and Ni^{2+}. The voltammograms of metallic ions from their various salts are shown in Fig. 12a–c. The copper-salt voltammogram revealed the complete two-step redox processes, namely, Cu^{2+}/Cu^{+} and Cu^{+}/Cu, while that of zinc salt revealed one complete forward- and backward-scan peak, indicating a Zn^{2+}/Zn redox process. Nickel salt showed only a single reduction step, indicating a Ni^{2+}/Ni process.

The voltammogram of **MJ_1** (Fig. 12d) showed that **MJ_1** is not electroactive as there appeared to be no redox process in both forward and backward scans. The cyclic voltammogram shown in Fig. 12e revealed two pairs of peaks as two distinct steps of reduction in the forward scan and oxidation in the reverse scan representing Cu^{2+}/Cu^{+} and Cu^{+}/Cu redox couples. The steps and potential values determined are as follows: step I corresponds to the Cu^{2+}/Cu^{+} redox pair with cathodic and anodic peak potentials of E_{pc}(I) = +200 mV and E_{pa}(I) = +850 mV, respectively; the peak separation ΔE_p(I) = 650 mV indicates a quasi-reversible behaviour;[56,57] step II corresponds to the Cu^{+}/Cu redox couple with cathodic and anodic peak potentials of E_{pc}(II) = −900 mV and E_{pa}(II) = −50 mV, respectively, with ΔE_p(II) = 850 mV. The latter process is metallic copper deposition during a cathodic scan with a characteristic stripping response on the anodic scan for copper dissolution. The shift in oxidation and reduction peaks indicated the complexation interaction of Cu^{2+} to **MJ_1**.

Fig. 12f also shows two pairs of peaks as two separate steps of reduction in the forward scan and oxidation in the reverse scan, representing Zn^{2+}/Zn^{+} and Zn^{+}/Zn redox couples. The steps and potential values displayed are as follows: step I corresponds to the Zn^{2+}/Zn^{+} redox pair with cathodic and anodic peak potentials

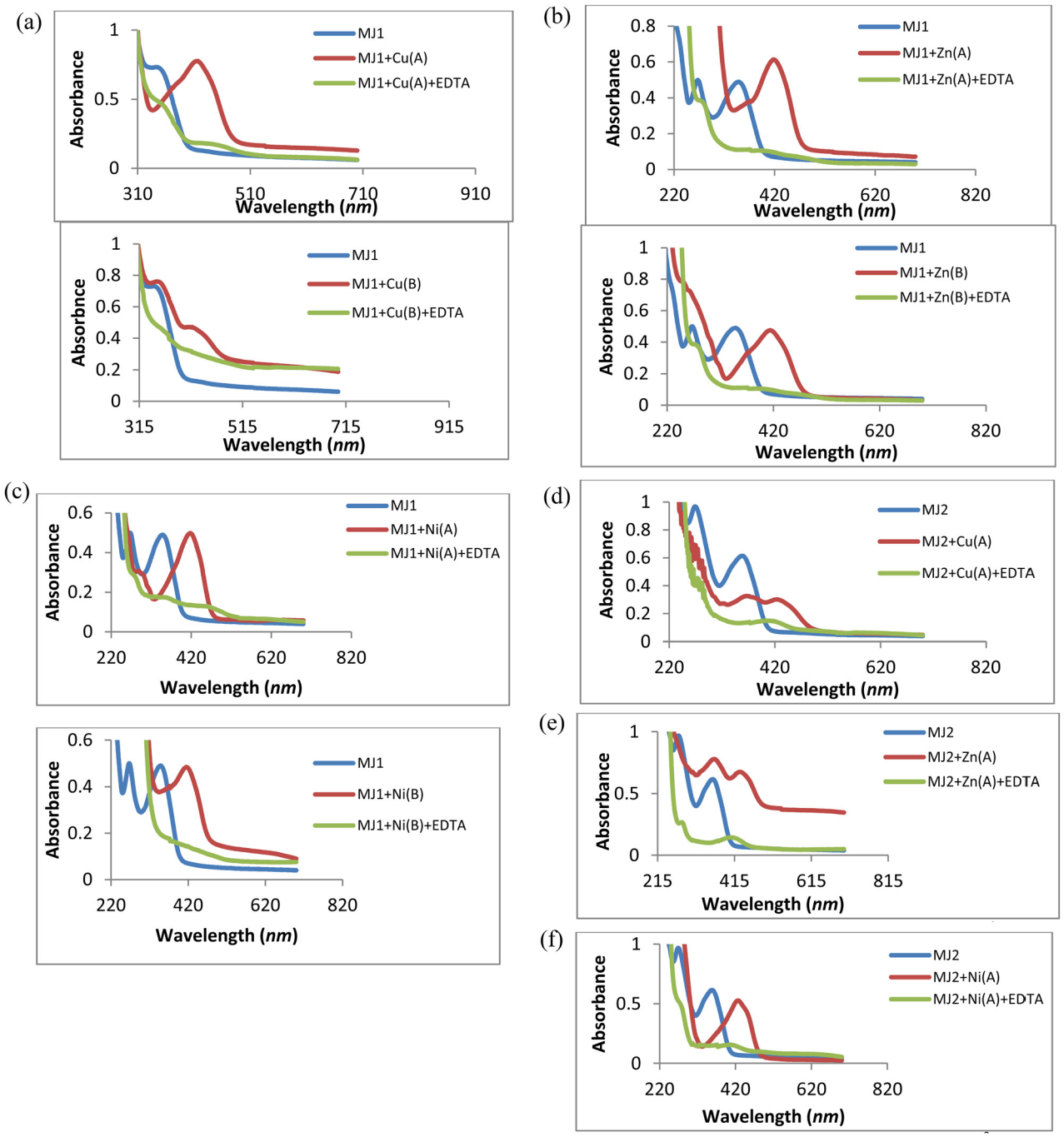

Fig. 11 (a) UV spectra of the reversibility studies of $\mathbf{MJ_1}$–Cu^{2+} complexes to free $\mathbf{MJ_1}$ using EDTA. (b) UV spectra of the reversibility studies of $\mathbf{MJ_1}$–Zn^{2+} complexes to free $\mathbf{MJ_1}$ using EDTA. (c) UV spectra of the reversibility studies of $\mathbf{MJ_1}$–Ni^{2+} complexes to free $\mathbf{MJ_1}$ using EDTA. (d) UV spectra of the reversibility studies of $\mathbf{MJ_2}$–Cu^{2+} complexes to free $\mathbf{MJ_2}$ using EDTA. (e) UV spectra of the reversibility studies of $\mathbf{MJ_2}$–Zn^{2+} complexes to free $\mathbf{MJ_2}$ using EDTA. (f) UV spectra of the reversibility studies of $\mathbf{MJ_2}$–Ni^{2+} complexes to free $\mathbf{MJ_2}$ using EDTA.

of $E_{pc}(I)$ = +100 mV and $E_{pa}(I)$ = +850 mV, respectively; the peak separation $\Delta E_p(I)$ = 750 mV indicates a quasi-reversible behavior; step II corresponds to the Zn^+/Zn redox couple with cathodic and anodic peak potentials of $E_{pc}(II)$ = –950 mV and $E_{pa}(II)$ = 250 mV, respectively, with $\Delta E_p(II)$ = 1200 mV. The latter step results in zinc deposition during a slow forward cathodic scan with a characteristic half-resolved peak response on the cathodic scan and subsequent fast dissolution exhibited by the well-resolved anodic peak. The slow dissolution from Zn/Zn^+ and Zn^+/Zn^{2+} redox processes was highly indicative of the good binding ability of $\mathbf{MJ_1}$ to Zn^{2+}. The shift in oxidation and reduction peaks is also indicative of the complexation of Zn^{2+} to $\mathbf{MJ_1}$.[58,59]

With regard to the interaction of Cr^{3+} with $\mathbf{MJ_1}$ (Fig. 12g), the voltammogram showed no significant photophysical changes.

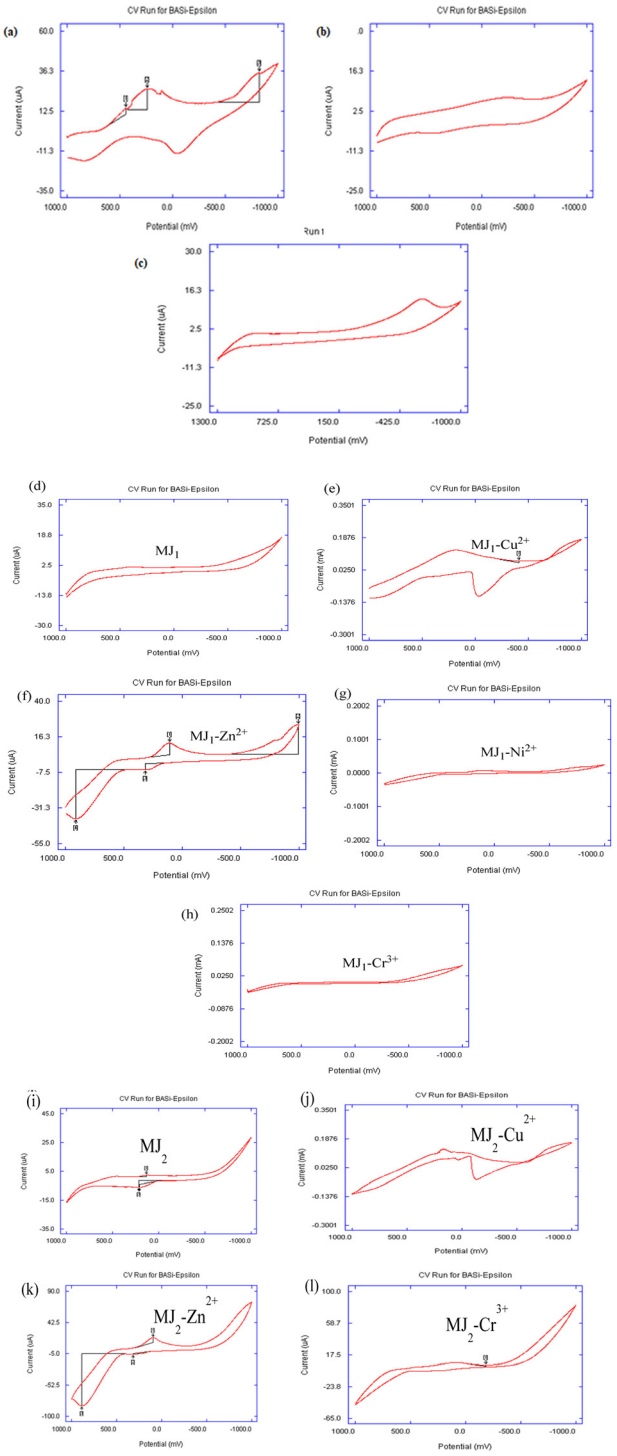

Fig. 12 (a–c) Cyclic voltammogram for 50 mM metallic ions in acetonitrile containing triethylammonium phosphate (TEAP) as a supporting electrolyte at a scan rate of 100 mV s^{-1}: (a) Cu^{2+}, (b) Zn^{2+}, and (c) Ni^{2+}. (d–h) Cyclic voltammogram for 25 mM **MJ_1** and its complexation with 50 mM metallic ions in acetonitrile containing TEAP as a supporting electrolyte at a scan rate of 100 mV s^{-1}: (d) **MJ_1**, (e) **MJ_1**–Cu^{2+}, (f) **MJ_1**–Zn^{2+}, (g) **MJ_1**–Cr^{3+}, and (h) **MJ_1**–Ni^{2+}. (i–l) Cyclic voltammogram for 25 mM **MJ_2** and its complexation with 50 mM metallic ions in acetonitrile containing TEAP as a supporting electrolyte at a scan rate of 100 mV s^{-1}: (i) **MJ_2**, (j) **MJ_2**–Cu^{2+}, (k) **MJ_2**–Zn^{2+}, and (l) **MJ_2**–Cr^{3+}.

This revealed a poor binding relationship between Cr^{3+} and **MJ_1**. The poorly resolved voltammogram shown in Fig. 12h also depicts a less noticeable binding interaction between Ni and **MJ_1**. The colorimetric feature of **MJ_1** in its binding with Cu, Zn, and Ni is also a revealing fact for the good probing feature of **MJ_1** for metals, while the observable non-change in the color noticed in the interaction of **MJ_1** with Cr^{3+} is supportive of the observed results, that is, the absence of the electro-activeness of **MJ_1** on the addition of Cr^{3+}.

Electrochemical behavior of MJ_2 with Cu^{2+}, Zn^{2+}, and Cr^{3+}. The voltammogram of **MJ_2** shown in Fig. 12i revealed that free **MJ_2** is electroactive as there appeared to be a complete one-electron redox process. The cyclic voltammogram shown in Fig. 12j revealed two pairs of peaks as two distinct steps of reduction in the forward scan and oxidation in the reverse scan, representing Cu^{2+}/Cu^{+} and Cu^{+}/Cu redox couples. The steps and potential values determined were as follows: step I corresponds to the Cu^{2+}/Cu^{+} redox pair with cathodic and anodic peak potentials of $E_{pc}(I)$ = +200 mV and $E_{pa}(I)$ = +800 mV, respectively, and the peak separation $\Delta E_p(I)$ = 600 mV indicates a quasi-reversible behavior; step II corresponds to the Cu^{+}/Cu redox couple with cathodic and anodic peak potentials of $E_{pc}(II)$ = −900 mV and $E_{pa}(II)$ = −100 mV, respectively, with $\Delta E_p(II)$ = 800 mV. The latter process results in metallic copper deposition during a cathodic scan with a characteristic stripping response on the anodic scan for copper dissolution. The shift in oxidation and reduction peaks indicated the complexation of Cu^{2+} to **MJ_2**.

In the voltammogram of **MJ_2**–Zn^{2+}, the forward scan exhibited a fast zinc-deposition reduction process involving Zn^{2+}/Zn. Here, Fig. 12k shows a pair of well-resolved quasi-reversible process. This cathodic peak and its anodic peak are indicative of a Zn^{2+}/Zn redox couple. The appearance of a slightly resolved irreversible anodic peak might indicate the slow formation of Zn^{+} during its dissolution after Zn deposition from the forward reduction scan. The steps and potential values displayed were as follows: step I corresponds to the Zn^{2+}/Zn redox pair with cathodic and anodic peak potentials of $E_{pc}(I)$ = +100 mV and $E_{pa}(I)$ = +880 mV, respectively, and the peak separation $\Delta E_p(I)$ = 780 mV indicates a quasi-reversible behaviour;[56,57] step II corresponds to the Zn/Zn^{+} oxidation with anodic peak potentials of $E_{pa}(II)$ = +325 mV. The shift in oxidation and reduction peaks is also indicative of the complexation of Zn^{2+} to **MJ_2**.

There appears to be a similarity in the binding characteristics between **MJ_1**–Cr^{3+} and **MJ_1**–Ni^{2+}, which was also observed for **MJ_2**–Cr^{3+} and **MJ_2**–Ni^{2+}. The voltammogram of **MJ_2**–Cr^{3+} (Fig. 12l) exhibited a reversible one-redox process, as also shown by **MJ_2** except for the change in peak current and resolution of peaks. This might indicate little or no binding interaction between Cr^{3+} and **MJ_2**.

Optical sensing. An optical sensing test of solutions of **MJ_1** after the addition of Cu^{2+}, Zn^{2+}, and Ni^{2+} salts showed significant color change detected by the naked eye. The color intensity gradually increased with higher concentrations of cupric ion, zinc ion, and nickel ion (Fig. 13a). Ligand **MJ_1** coordinated with Cu^{2+}, Zn^{2+}, and Ni^{2+} to form stable complexes, resulting in a

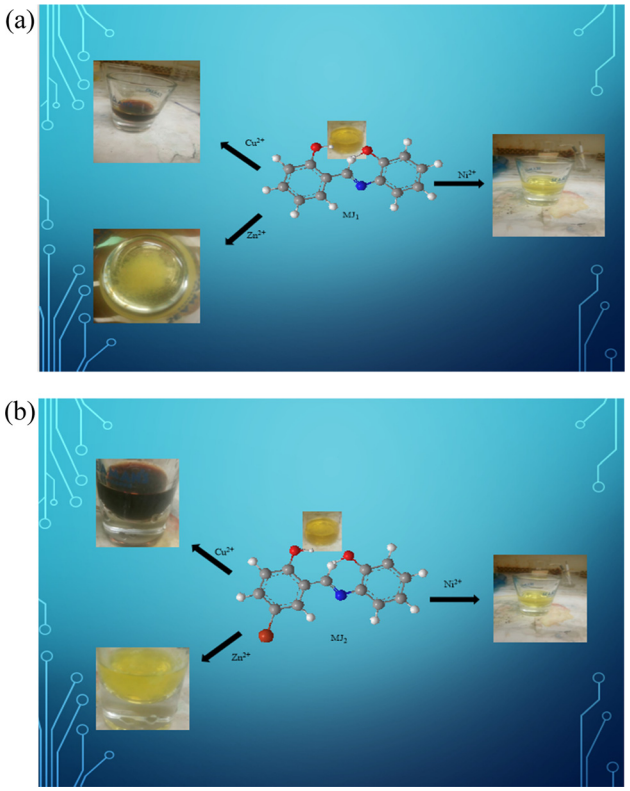

Fig. 13 (a) Colorimetric response of $\mathbf{MJ_1}$ upon the addition of Cu^{2+}, Zn^{2+}, and Ni^{2+}. (b) Colorimetric response of $\mathbf{MJ_2}$ upon the addition of Cu^{2+}, Zn^{2+}, and Ni^{2+}.

decrease in the intensity of its UV-vis spectrum and a redshift. This can be attributed to the formation of $\mathbf{MJ_1}$–Cu^{2+}, $\mathbf{MJ_1}$–Zn^{2+}, and $\mathbf{MJ_1}$–Ni^{2+} complexes. Further, this could be the result of a lone pair of electrons on the phenolic group and the imine group in the chromophore, which may perpendicularly bind to the metals located in the cavity of $\mathbf{MJ_1}$.

Furthermore, the optical sensing of $\mathbf{MJ_2}$ solutions on the addition of Cu^{2+}, Zn^{2+}, and Ni^{2+} salts also showed significant color changes. The solution mixtures gradually changed from orange to reddish brown, deep yellow, and yellow, respectively (Fig. 13b). This change was detected by the naked eye. The color intensity also gradually decreased with a lower concentration of metal ions.

Computational studies

Geometry optimization of $\mathbf{MJ_1}$–Cu^{2+} and $\mathbf{MJ_2}$–Cu^{2+} complexes. To complement the experimental results, DFT calculations were performed on the chemo-sensors and their Cu complexes. The optimized geometry of ligands $\mathbf{MJ_1}$ and $\mathbf{MJ_2}$ and the proposed structures of their complexes, CuCl–$\mathbf{MJ_1}$ and CuCl–$\mathbf{MJ_2}$, are displayed in Fig. 14 with some geometric parameters. Various structures were proposed for the complexes; the structures of the displayed complexes are based on the experimentally observed UV-vis spectra *vide supra*, which corresponds to a square planar complex and also the known binding mode of the Schiff bases.[60–62] A slight variation is

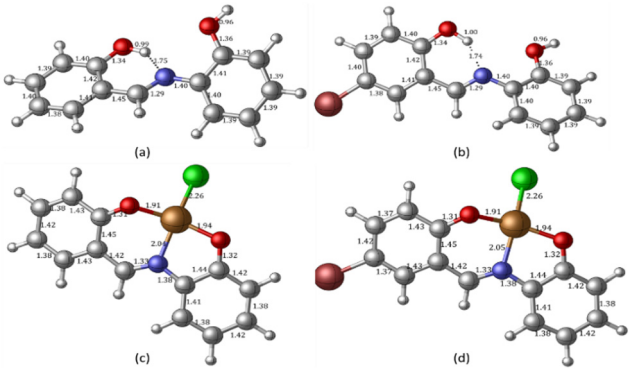

Fig. 14 DFT-optimized geometry of free Schiff bases (a) $\mathbf{MJ_1}$ and (b) $\mathbf{MJ_2}$ obtained at the B3LYP/6-311++G(d,p) level of theory and their copper complexes obtained at the B3LYP/LANL2DZ level of theory: (c) complexed $\mathbf{MJ_1}$–Cu^{2+} and (d) complexed $\mathbf{MJ_2}$–Cu^{2+}.

observed with the known crystal structure[62] compared with $\mathbf{MJ_1}$, where the ligand is planar and Cu atom is slightly displaced; here, the copper atom is more displaced out of plane. This is believed to be due to the absence of other interactions that are usually present in the crystal structure, particularly π–π stacking, which is absent in single-molecule optimization. The optimized structures of the ligands are in line with their crystal structure obtained for $\mathbf{MJ_1}$[62] where the OH group on the aminophenol moiety is directed away from the amino group as it is involved in the intermolecular hydrogen bond with another molecule in the lattice. Due to its accuracy and low computational cost, time-dependent density functional theory (TDDFT) has been extensively used to calculate the molecular properties such as electronic, structural, and magnetic properties, and it gives results similar to the experimental results. The TDDFT theoretical spectra obtained at the same level of theory as used in optimization are given in Fig. 15 and summarized in Table 2 along with the experimentally observed peaks.

The two predominant peaks of 271.91 and 351.38 nm for $\mathbf{MJ_1}$ and 271.50 and 364.44 nm for $\mathbf{MJ_2}$ that can be attributed to the

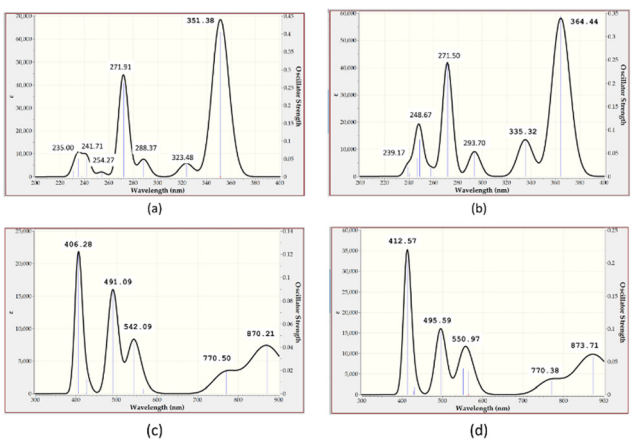

Fig. 15 Computed UV-vis absorption spectrum of (a) $\mathbf{MJ_1}$, (b) $\mathbf{MJ_2}$, (c) $\mathbf{MJ_1}$–Cu^{2+}, and (d) $\mathbf{MJ_2}$–Cu^{2+} complexes.

Table 2 Summary of transitions from DFT-computed UV spectra of optimized free ligands **MJ$_1$** and **MJ$_2$** at the B3LYP/6-311++G(d,p) level of theory and the experimental UV spectra

	MJ$_1$		**MJ$_2$**			
Transitions	Computed (nm)	Expt. (nm)	Computed (nm)	Expt. (nm)	**MJ$_1$**–Cu^{2+}	**MJ$_2$**–Cu^{2+}
$\pi \rightarrow \pi^*$	271.91	271	271.50	274		
$n \rightarrow \pi^*$	351.36	352	364.44	363		
					406.28	412.57

$\pi \rightarrow \pi^*$ and $n \rightarrow \pi^*$ transitions, respectively, in the experimental absorption spectra are at about 271, 352, 274, and 363 nm in both **MJ$_1$** and **MJ$_2$** and a corresponding result is obtained from the computational studies. The calculated UV-vis spectra of the metal complexes are also reported in the range of 400–900 nm and compared with the experimental values. The peaks at about 406.28 nm for the **MJ$_1$**–Cu^{2+} complex and 412.57 nm for **MJ$_2$**–Cu^{2+} complex are close to the experimental values of around 415–434 nm for both complexes (Fig. 9a and 10a; *vide supra*). The line obtained at around 870 nm is also closely related to a copper complex of a similar ligand reported in the literature,[60] which further confirms the square planar structure predicted for the complex.

Theoretical electronic properties of MJ$_1$, MJ$_2$, MJ$_1$–Cu^{2+}, and MJ$_2$–Cu^{2+}. To gain a clear understanding of the chemo-sensing mechanism (energy and/or charge transfer) of **MJ$_1$** and **MJ$_2$** in the presence of Cu^{2+}, the frontier molecular orbitals, highest-occupied molecular orbital (HOMO), lowest-unoccupied molecular orbital (LUMO), and orbital next to the LUMO, *i.e.*, LUMO+1 of both free ligands and their copper complexes were studied. These frontier molecular orbitals have been shown to adequately describe the chemical reactivities of small compounds.[63–65] These are displayed along with their energy values (Fig. 16 and 17, respectively) for the ligands and their complexes.

The energy difference between the HOMO and LUMO, E_{LUMO}–E_{HOMO} and between the LUMO and LUMO+1 is 4.012 and 1.456 eV (**MJ$_1$**) and 3.874 and 1.519 eV (**MJ$_2$**), respectively. These energy gaps have been significantly quenched by complex formation with Cu^{2+} where the HOMO–LUMO energy gaps of **MJ$_1$**–Cu^{2+} and **MJ$_2$**–Cu^{2+} complexes have been reduced to 1.877 and 1.872 eV, respectively. The decrease in the energy gap clearly confirms the strong ligand–metal interaction between sensors **MJ$_1$** and **MJ$_2$** and the Cu^{2+} cation. It is also noted that the electron density is evenly distributed over the whole molecule for both free Schiff bases at both HOMO and LUMO and localized on the aminophenol moiety at LUMO+1 for **MJ$_1$**. Upon complexation, the electronic distribution is mostly localized on the metal and hydroxyl benzylidene moiety of the ligand at both HOMO and LUMO, with a reduced orbital coefficient on the aminophenol moiety. However, LUMO+1 has a negligible orbital coefficient on the Cu atom in both complexes and is mostly a ligand orbital and can be referred to as non-bonding. From TDDFT analysis, the prominent bands at 406.28 eV (**MJ$_1$**–CuCl) and 412.51 eV (**MJ$_2$**–CuCl) is majorly a transition from HOMO to LUMO+1, which represents a metal-to-ligand charge transfer. Other transitions are intramolecular charge transfer within the ligand as well as metal-to-ligand charge transfer (Fig. S2–S6 and S8–S12, ESI†). Therefore, the sensing mechanism of **MJ$_1$** and **MJ$_2$** to Cu^{2+} might be explained by metal-to-ligand charge transfer and LMCT mechanisms between the orbitals of the ligands and metal. The push–pull effect of the electron-donating and electron-withdrawing groups leading to a redshift, that is, binding metal ions to the electron-withdrawing moieties, indicates a decrease in the energy gap.[66]

The energy values of HOMO and LUMO were also used to describe the global reactivity descriptors of the sensors (**MJ$_1$** and **MJ$_2$**) as defined within the DFT framework by Parr and additional works from Gázquez *et al.*[66] and Chattaraj *et al.*[67] These are global hardness (η), global softness (S), chemical potential (μ), electronegativity (X), electrophilicity

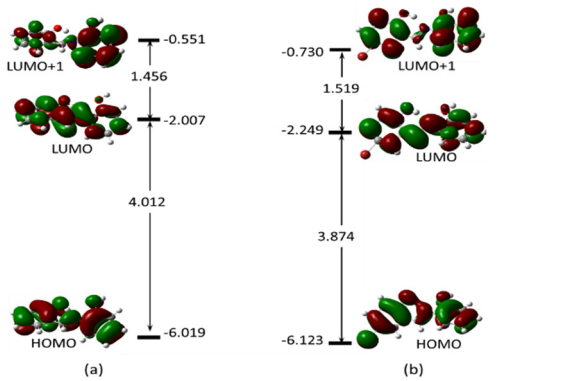

Fig. 16 Electron density map of the frontier orbitals of (a) **MJ$_1$** and (b) **MJ$_2$** showing their energy eigenvalues in eV and the energy gap between them.

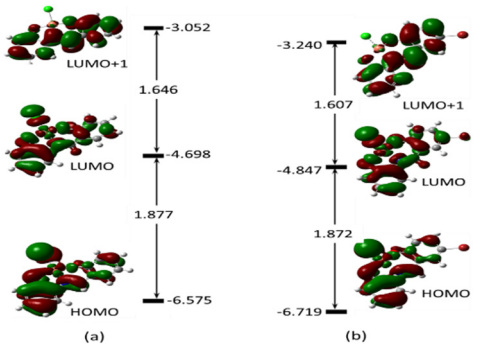

Fig. 17 Electron density map of the frontier orbitals of (a) **MJ$_1$**–Cu^{2+} and (b) **MJ$_2$**–Cu^{2+} showing their energy eigenvalues in eV and the energy gaps between them to show the intermolecular charge transfer or photoinduced charge transfer (PCT) mechanism during complexation.

Table 3 Chemical reactivity descriptor of free MJ_1 and MJ_2 ligands and their dipole moment

Ligand	MJ_1	MJ_2
E_{LUMO} (eV)	−2.007	−2.249
E_{HOMO} (eV)	−6.019	−6.123
ΔE_{gap} (eV)	4.012	3.874
I (eV)	6.019	6.123
A (ev)	2.007	2.249
η (eV)	2.006	1.937
S (eV)	0.499	0.516
μ (eV)	−4.013	−4.186
χ (eV)	4.013	4.186
ω^- (eV)	8.026	8.385
ω^+ (eV)	4.517	5.345
$\Delta\omega^+$(eV)	12.5431	13.729
μ_D (D)	2.59	3.66
I (eV)	6.019	6.123

index (ω) (electron-donating power (ω^-), electron-accepting power (ω^+) and net electrophilicity ($\Delta\omega^{\pm}$)), and ionization potential (I) and are given along with their dipole moment (μ_D) (Table 3). With these, we can discuss the effect of bromine atom on the salicylaldehyde moiety. A wider HOMO–LUMO gap often indicates a more stable molecule. It is noted that the Br atom on the salicylaldehyde moiety in MJ_2 narrows the HOMO–LUMO gap by lowering E_{LUMO} more than E_{HOMO}, and maybe less stable compared to MJ_1 and may be more reactive.

It is also noted that MJ_1 is chemically softer than MJ_2. A larger value of ω^+ corresponds to a larger capability of accepting charges, whereas a smaller value of ω^- implies a larger capability of donating charges. We note that MJ_2 has more electron-accepting abilities and net electrophilicity than MJ_1 from their net electrophilicity values, *i.e.*, the electron-accepting power relative to the electron-donating power as defined in eqn (1).[67]

$$\Delta\omega^{\pm} = \omega^+ + \omega^- \quad (1)$$

From the resolved forward- and backward-scan peaks (Fig. 12d and i), MJ_2 has a better electrochemical activity than MJ_1. Further, from the UV absorption-peak intensities, we can say that MJ_2 attenuates light better than MJ_1, as revealed by the energy-gap values. This suggests substituents that lower E_{LUMO} will most likely give a better sensor, as seen in MJ_2.

Molecular electrostatic potential (MEP) map. The molecular electrostatic potential (MEP) surfaces mapped over the total density of the geometrically optimized free ligands and their complexes are displayed in Fig. 18. MEP maps generated in space around a molecule by charge distribution are used to understand the electrophilic or nucleophilic properties, and provide information regarding the chemical reactivity of a molecule represented by various colors. The range in color from the region of red to blue represents the increase in negativity of the surface, *i.e.*, the red areas of the map are negatively charged surfaces and depict area of nucleophilic attack on the molecular surface and blue areas are positively charged surfaces prone to electrophilic attack; the green area represents regions of zero potential. From Fig. 18a and b, it is evident that the most positive area on the surface is the

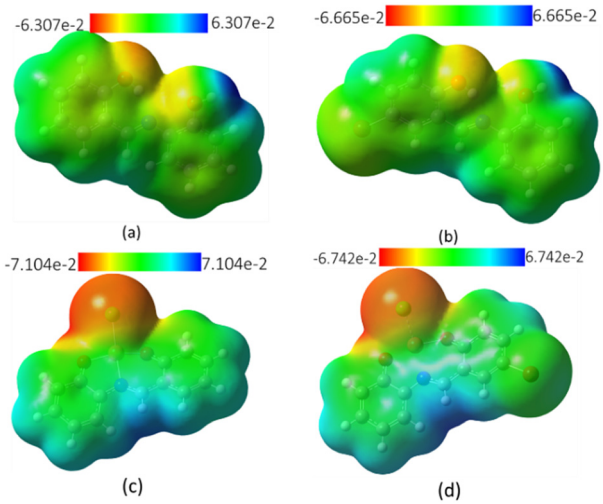

Fig. 18 MEP showing the electron density of molecules of (a) MJ_1, (b) MJ_2, (c) MJ_1–Cu^{2+}, and (d) MJ_2–Cu^{2+}.

hydrogen atom on the hydroxyl group on the aminophenol moiety, while the surface around the oxygen atoms, particularly on the salicylaldehyde, represent the area for electrophilic attack and is therefore susceptible to complexation with Cu^{2+} electrophile. Upon complexation, the most positive charge is now the area around the hydrogen atom on the nitrogen atom (Fig. 18c and d).

Atomic charge analysis. The structural or molecular properties have direct relationship with the polarizability property of the molecule, kinetic stability, hydrogen-ion donor and acceptor ability, dipole moment, and other physical and chemical properties.[62] Atomic charges being an important molecular parameter gives information on some of these properties. In the complexation of metals and ligands, the charges on the ligand moieties and metal ions possibly help to reveal the possible binding interaction sites between the ligands and metal ions. The Mulliken Population Analysis (MPA) method has been widely used for determining atomic charges, although it is basis set dependent.[68] A pictorial representation of the

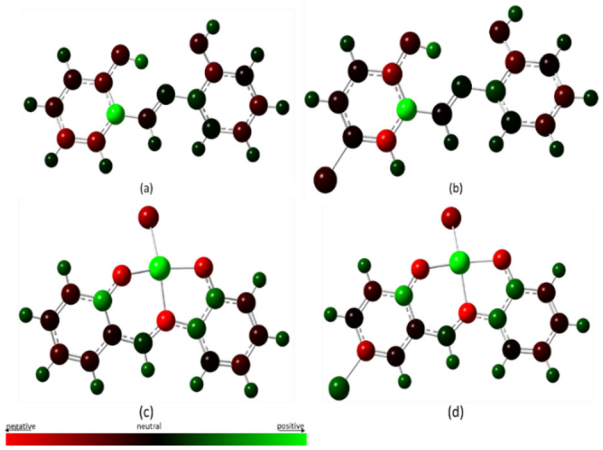

Fig. 19 MAC distribution for the free ligand and their copper complexes.

Table 4 MAC values of atoms in free ligands **MJ₁** and **MJ₂** and their copper complexes

		MJ₁	**MJ₁**–Cu^{2+}	**MJ₂**	**MJ₂**–Cu^{2+}
1	C	−0.5415	−0.1292	−0.8913	−0.0682
2	C	−0.5824	−0.1692	−0.0989	−0.4338
3	C	−0.2180	−0.0902	−0.1263	−0.0362
4	C	1.1278	−0.0837	1.1420	−0.0759
5	C	−0.3727	0.3925	−0.6189	0.4024
6	C	−0.1915	−0.1729	−0.0928	−0.1643
7	C	−0.1381	0.1028	−0.0408	0.1025
8	N	0.0685	−0.6758	0.0737	−0.6727
9	C	0.2008	0.2344	0.2352	0.2341
10	C	0.0589	−0.0355	0.0461	−0.0347
11	C	−0.2888	−0.1710	−0.2686	−0.1697
12	C	−0.3778	0.2519	−0.3915	0.2525
13	C	−0.3180	−0.1103	−0.3243	−0.1093
14	C	−0.0538	−0.1415	−0.0568	−0.1401
15	H	0.1188	0.2009	0.1113	0.2028
16	H	0.1516	0.1668	0.2249	0.1877
17	H	0.1687	0.1701	0.2225	0.1906
18	H	0.1796	0.1985	0.1884	0.2040
19	H	0.1494	0.1801	0.1489	0.1819
20	H	0.1369	0.1956	0.1390	0.1974
21	H	0.1730	0.1663	0.1757	0.1684
22	H	0.1569	0.1711	0.1591	0.1730
23	O	−0.2953	−0.5454	−0.2932	−0.5422
24	O	−0.2083	−0.5099	−0.2080	−0.5081
25	X_1[a]	0.4755	0.4791	0.4750	0.6442
26	X_2[b]	0.2614	−0.4070	0.2630	−0.4020
27	R[c]	0.1584	0.1655	−0.1975	0.2157

[a] X_1 is H in the ligand and Cu in the complex. [b] X_2 is H in the ligand and Cl in the complex. [c] R is H in **MJ₁** and Br in **MJ₂**.

Mulliken Atomic Charge (MAC) distribution is given in Fig. 19 and the numerical values of the charges are listed in Table 4. The green color indicates positive charges and centers for nucleophilic attack, the red color indicates negative charges, and the neutral color is indicated in darker shades. From the table, it is evident that there is increased electron density on the nitrogen atom after complexation, from 0.0685 (**MJ₁**) and 0.00737 (MJ_2) to −0.6758 (**MJ₁**–Cu^{2+}) and −0.6227 (**MJ₂**–Cu^{2+}). A similar trend is seen in the oxygen atoms and C_4 as well with increased electron density. This further corroborates the metal-to-ligand charge transfer upon complexation.

Conclusions

We have successfully developed 2-aminophenol-based Schiff base chemo-sensors **MJ₁** and **MJ₂** for the detection of Cu^{2+} and Zn^{2+}. **MJ₁** and **MJ₂** could be employed as a low cost and ultra-sensitive colorimetric sensor to detect and determine Cu^{2+} and Zn^{2+} in the range from 9.75×10^{-6} to 2.5×10^{-3} mol dm^{-3}, which is considered to be a low detection limit; this is lower than the WHO-recommended amount in drinking water. The observed photochemical and electrochemical results showed that the chemo-sensors **MJ₁** and **MJ₂** have good binding interaction with Cu^{2+} and Zn^{2+} and suggests an ICT (LMCT) binding association. DFT calculations were used to determine the geometry of the complex formed with copper (based on the UV-vis screening of the complex formed), which is a square planar complex. TDDFT analysis and charge analysis showed LMCT and back-donation to ligand. The bromine atom on **MJ₂** lowers both HOMO and LUMO energy levels, making it more electron accepting to the metal complex.

Experimental

Reagents

The chemicals and reagents used were purchased from Sigma-Aldrich Chemical Co. Ltd and used without further purification. They include ethanol, 2-aminophenol, salicylaldehyde, 5-bromosalicylaldehyde, copper(II) chloride dehydrate ($CuCl_2 \cdot 2H_2O$), zinc nitrate hexahydrate ($Zn(NO_3)_2 \cdot 6H_2O$), nickel chloride hexahydrate ($NiCl_2 \cdot 6H_2O$), chromium chloride hexahydrate ($CrCl_3 \cdot 6H_2O$), iron(III) chloride hexahydrate ($FeCl_3 \cdot 6H_2O$), TEAP, acetonitrile, and acetone.

Apparatus

The melting points of all the synthesized compounds were determined using the Stuart melting point apparatus model in the Chemistry Department of the University of Lagos, Nigeria. Infrared (FTIR) spectra of the compounds were recorded on the spectrum in the range of 4000 to 400 cm^{-1} using a Bruker FTIR model alpha spectrophotometer at the Chemistry Department of the University of Ibadan, Nigeria. The electronic absorption data were recorded on a Shimadzu PGT80/T80+ UV-vis spectrophotometer using 1×10^{-5} M acetonitrile solution in a 1 cm quartz cell at room temperature. The synthesis reactions were monitored by a TLC instrument. The ^1H NMR spectra were collected in deuterated methanol and referenced to the residual protonated solvent peak of 3.31 ppm using a Bruker 600 MHz Avance III HD spectrometer, and electrospray ionization (ESI) mass spectrometry was completed in the positive or negative mode as indicated with methanol as the eluent using a Bruker Impact LC-MS at the Department of Chemistry and Biochemistry, Ohio State University, Columbus, USA. The electrochemical studies were performed using a platinum electrode as the auxiliary electrode, glassy carbon electrode (GCE) as the working electrode, and Ag/AgCl electrode as the reference electrode using Epsilon Ec. Vet. 213.77 Xp voltammetry machine at the Chemistry Department of the University of Lagos. Electrochemical parameters: Epsilon Ec. Vet. 213.77 Xp, Scan rate (mV s^{-1}): 100 mV; number of segments: 2; quiet time (s): 2; scale: 100 mA and 1 mA; reference electrode (Ag/AgCl electrode), working electrode (GCE), counter electrode (platinum electrode), supporting electrolyte (TEAP); solvent, acetonitrile.

Synthesis

Synthesis of (*Z*)-2-((2-hydroxybenzylidene)amino)phenol (MJ₁). To a stirred ethanolic solution of 10 mL of 2-aminophenol (5 mmol, 0.5455 g), 10 mL ethanolic solution of salicylaldehyde (5 mmol, 0.585 g) was added. The reaction mixture was then kept under reflux for 6 h at 70 °C. The reaction was monitored by a TLC using (4 : 1) *n*-hexane and ethyl acetate solvent system. The mixture was cooled to room temperature and the red product obtained was collected by filtration and recrystallized using

ethanol. This afforded a red crystalline compound **MJ_1**. Yield: 63.18%; melting point: 188–190 °C; IR (cm^{-1}): 3173, 2343, 1630, 1613, 1592, 1529, 1463, 1222, 1139, 725; ^{1}H NMR (600 MHz, CD_3OD): d 8.88 (s, 1H, −HC = N), 7.50 (dd, 1H, J = 7.7, 1.6, −ArH), 7.36 (td, 1H, J = 7.9, 1.8, −ArH), 7.30 (dd, 1H, J = 7.9, 1.5, −ArH), 7.12 (td, 1H, J = 7.6, 1.6, −ArH), 6.92 (q, 1H, J = 8.6, −ArH); ESI-MS calculated for $C_{13}H_{11}NO_2$ $[M + 1H]^{+1}$ m/z = 214.08, found 214.09.

Synthesis of (*Z*)-4-bromo-2-(((2-hydroxyphenyl)imino)methyl)-phenol (MJ_2). To a stirred ethanolic solution of 10 mL of 2-aminophenol (5 mmol, 0.5455 g), 10 mL ethanolic solution of 5-bromosalicylaldehyde (5 mmol, 1.0051 g) was added. The reaction mixture was then kept under reflux for 6 h at 70 °C. The reaction was monitored by a TLC using (4 : 1) *n*-hexane and ethyl acetate solvent system. The mixture was cooled to room temperature and the yellow product obtained was collected by filtration and recrystallized using ethanol. This afforded a yellow crystalline compound **MJ_2**. Yield: 67.10%; melting point: 190–192 °C; IR (cm^{-1}): 3028, 2344, 1628, 1591, 1526, 1509, 1128, 755; ^{1}H NMR (600 MHz, CD_3OD): d 8.87 (s, 1H, −HC = N), 7.67 (d, 1H, J = 2.5, −ArH), 7.44 (dd, 1H, J = 8.9, 2.6, −ArH), 7.33 (dd, 1H, J = 8.0, 1.6, −ArH), 7.14 (td, 1H, J = 7.8, 1.5, −ArH), 6.94 (dd, 1H, J = 8.2, 1.2, −ArH), 6.91 (td, 1H, J = 7.5, 1.3, −ArH), 6.86 (d, 1H, J = 8.9, −ArH); ESI-MS calculated for $C_{13}H_{10}BrNO_2$ $[M - 1H]^{-1}$ m/z 289.99, found 289.98.

UV-vis absorption spectroscopy study

Preparation and measurement of Schiff bases MJ_1, MJ_2 solutions. Here, 0.01 mmol of each of the ligand was dissolved in 2 mL acetonitrile. Then, 20 μl of the ligand solutions was diluted with 3 mL acetonitrile to make a final concentration of 33 μM (3.02 mL). UV-vis spectra were recorded from 200 to 800 nm.

UV-vis titration measurements. 0.04 mmol of copper chloride dihydrate ($CuCl_2{\cdot}2H_2O$) was dissolved in bis–tris buffer (2 mL). Then, 0.2, 0.4, 0.6, 0.8, and 1.0 mL of Cu solution was added to each of the prepared Schiff base (**MJ_1** and **MJ_2**) solutions. The titration solutions were analyzed using absorption spectroscopy.

The same procedure was repeated for each of zinc nitrate hexahydrate ($Zn(NO_3)_2{\cdot}6H_2O$), nickel chloride hexahydrate ($NiCl_2{\cdot}6H_2O$), chromium chloride hexahydrate ($CrCl_3{\cdot}6H_2O$), and iron(III) chloride hexahydrate ($FeCl_3{\cdot}6H_2O$) salts.

Reversibility test of MJ_1–Cu^{2+} and MJ_1–Zn^{2+} to MJ_1 using EDTA receptor

MJ_1 (1.06 mg, 0.005 mmol) was dissolved in acetonitrile (2 mL) and 15 μL (2.5 μM) of it was diluted with 2.985 mL acetonitrile buffer solution (1 : 5, v/v, 10 mM, bis–tris, pH 7.0) to make a final concentration of 12.5 μM. $CuCl_2.2H_2O$ (1.70 mg, 0.01 mmol) was dissolved in acetonitrile (2 mL) and 3.2 mL of the Cu^{2+} solution (5 mM) was added to the solution of **MJ_1** (12.5 μM) prepared above. The solutions were mixed for 30 s, and the UV-vis spectrum was taken at room temperature. Ethylenediaminetetraacetic acid (EDTA, 0.04 mmol) was dissolved in a buffer solution (2 mL) and 0.2 mL of the EDTA solution (20 mM) was added to the solution of **MJ_1**–Cu^{2+} complex. After mixing for 1 min, the UV-vis spectrum was taken. The addition of 0.2 mL EDTA solution (20 mM) was done in duplicate.

Electrochemical studies

Electrochemical study of MJ_1 and MJ_2 with Cu(II), Zn(II), Ni(II), and Cr(III) ions. A solution of TEAP (0.0231 g) was prepared in 100 mL acetonitrile. Then, 10 mL TEAP solution for each of **MJ_1** and **MJ_2** (0.25 mmol) was prepared. Thereafter, 5 mL of each of the prepared solutions was electrochemically analyzed using cyclic voltammetry. Subsequently, 5 mL TEAP solution of a metal salt (0.25 mmol) was added for complexation. These mixtures were also electrochemically screened using cyclic voltammetry. The voltammetric scan of the TEAP solution of metal salt alone was also carried out.

Optical sensing test

The optical sensing test of the solutions of receptors **MJ_1** and **MJ_2** (0.01 mmol) in 2 mL MeCN after the addition of Cu^{2+}, Zn^{2+}, and Ni^{2+} salts (0.02 mmol) showed significant colour changes.

Theoretical studies of MJ_1, MJ_2, and their complexes

Computational details. The geometry optimization of the Schiff base chemo-sensor and their copper complexes were carried out without constraints using the density functional B3LYP,[69] as described within the GAUSSIAN 09W[70] software suite. The 6-311g++(d,p)[71] people-type basis set was used for the free Schiff base and for the LANL2DZ[72] complex along with its ECP was used for the copper atom, while the 6-311g++(d,p) functional was used for the other atoms in the complex. Frequency calculation at the same level of theory as geometry optimization was used to ascertain that a true minimum was obtained without any negative eigenvalue. Gaussview5.0 software,[73] a graphical user interface for GUASSIAN09, was used to generate the structures for optimization; it was also used to generate the molecular orbital and electrostatic potential maps. The CYLview[74] visualization software was used to generate the optimized structure. The TDDFT method has been used to study the wavelengths (λ_{max}), excitation vertical energy, and corresponding oscillator strengths.

Global reactivity descriptors like chemical hardness (η), electronic chemical potential (μ), electronegativity (χ), global softness (S), and electrophilicity index (ω) were derived from the energy of HOMO and LUMO, namely, E_{HOMO} and E_{LUMO}, respectively. Within the framework of finite-differences approximation, the global reactivity descriptors were calculated as follows.[75–78]

$$I = -E_{HOMO} \quad (2)$$

$$A = -E_{LUMO} \quad (3)$$

$$\eta = -\frac{E_{HOMO} - E_{LUMO}}{2} \quad (4)$$

$$\mu = \frac{E_{HOMO} + E_{LUMO}}{2} \quad (5)$$

$$\omega = \frac{\mu^2}{2\eta} \tag{6}$$

$$\chi = -\mu = -\frac{E_{\mathrm{HOMO}} + E_{\mathrm{LUMO}}}{2} \tag{7}$$

$$S = 1/2\eta \tag{8}$$

$$\omega^- \approx \frac{(3I + A)^2}{16(I - A)}$$

$$\omega^+ = \frac{(I + 3A)^2}{16(I - A)} \tag{9}$$

$$\Delta\omega^{\pm} = \omega^+ + \omega^- \tag{10}$$

Author contributions

Felicia N. Ejiah, Mujeeb O. Rofiu and Tolulope M. Fasina designed the experiments and carried out the analysis. Oluwakemi A. Oloba-Whenu and Mujeeb O. Rofiu carried out the computational studies and analysis. Felicia N. Ejiah, Mujeeb O. Rofiu, Oluwakemi A. Oloba-Whenu and Tolulope M. Fasina interpreted the results and wrote the manuscript. All authors have read and approved the final manuscript.

Conflicts of interest

There are no conflicts of interest to declare.

Acknowledgements

Thanks are due to Prof. Claudia Turro and Jessie Vandevord of the Department of Chemistry and Biochemistry, Ohio State University who assisted in analysis of the ligands using ESI-MS and NMR.

References

1 R. Pandey, A. Kumar, Q. Xu and D. S. Pandey, *Dalton Trans.*, 2020, **49**, 542.
2 F. Wang, L. Wang, X. Chen and J. Yoon, *Chem. Soc. Rev.*, 2014, **43**, 4312.
3 K. Kaur, R. Saini, A. Kumar, V. Luxami, N. Kaur, P. Singh and S. Kumar, *Coord. Chem. Rev.*, 2012, **256**, 1992.
4 L. H. Abdel-Rahman, A. M. Abu-Dief and A. A. H. Abdel-Mawgoud, *Ann. Chem. Sci. Res.*, 2019, **1**, 1.
5 L. H. Abdel-Rahman, A. M. Abu-Dief and A. A. H. Abdel-Mawgoud, *Int. J. Nano. Chem.*, 2019, **5**, 1.
6 J. M. V. Ngororabanga, C. Moyo, E. Hosten, N. Mama and Z. R. Tshentu, *Anal. Methods*, 2019, **11**, 3857.
7 X. Chen, X. Tian, I. Shin and J. Yoon, *Chem. Soc. Rev.*, 2011, **40**, 4783.
8 E. Persch, O. Dumele and F. Diederich, *Angew. Chem., Int. Ed.*, 2015, **54**, 3290.
9 H. Xiang, J. Cheng, X. Ma, X. Zhou and J. J. Chruma, *Chem. Soc. Rev.*, 2013, **42**, 6128.
10 Y. V. Tcherkas and A. D. Denisenko, *J. Chromatogr. A*, 2001, **913**, 309.
11 J. S. Becker, A. Matusch, C. Depboylu, J. Dobrowolska and M. V. Zoriy, *Anal. Chem.*, 2007, **79**, 6074.
12 M. M. Sanagi, A. A. Naim, W. A. Wan Ibrahim and U. Baig, *Anal. Methods*, 2015, **7**, 3215.
13 M. Faraji, Y. Yamini and S. Shariati, *J. Hazard. Mater.*, 2009, **166**, 1383.
14 Y. Liu, P. Liang and L. Guo, *Talanta*, 2005, **68**, 25.
15 O. Nekrassova, N. S. Lawrence and R. G. Compton, *Talanta*, 2003, **60**, 1085.
16 N. Pourreza and R. Hoveizavi, *Anal. Chim. Acta*, 2005, **549**, 124.
17 L. M. Laglera and D. Monticelli, *Curr. Opin. Electrochem.*, 2017, **3**, 123.
18 A. A. Ensafi, T. Khayamian, A. Benvidi and E. Mirmomtaz, *Anal. Chim. Acta*, 2006, **561**, 225.
19 S. Omarova, S. Demir and M. Andac, *J. Taibah Univ. Med. Sci.*, 2018, **12**, 820.
20 S. D. Gower-Winter and C. W. Levenson, *BioFactors*, 2012, **38**, 186.
21 C. J. Frederickson, J. Y. Koh and A. I. Bush, *Nat. Rev. Neurosci.*, 2005, **6**, 449.
22 S. Gol, R. N. Pena, M. F. Rothschild, M. Tor and J. Estany, *Sci. Rep.*, 2018, **8**, 1.
23 P. Paoletti, A. M. Vergnano, B. Barbour and M. Casado, *Neuroscience*, 2009, **158**, 126.
24 S. D. Portbury and P. A. Adlard, *Int. J. Mol. Sci.*, 2017, **18**, 2506.
25 J. M. Goldberg, F. Wang, C. D. Sessler, N. W. Vogler, D. Y. Zhang, W. H. Loucks and S. J. Lippard, *J. Am. Chem. Soc.*, 2018, **140**, 2020.
26 E. Castagnola, E. M. Robbins, K. M. Woeppel, M. McGuier, A. Golabchi, I. M. Taylor and X. T. Cui, *Front. Bioeng. Biotechnol.*, 2020, **8**, 602216.
27 Y. S. Kim, G. J. Park, S. A. Lee and C. Kim, *RSC Adv.*, 2015, **5**, 31179.
28 S. K. Shinde, D. P. Dubal, G. S. Ghodake, D. Y. Kim and V. J. Fulari, *Nano-Struct. Nano-Objects*, 2016, **6**, 5.
29 Federal Register, Rules and Regulations, 2000, 65, **www.govinfo.gov/content/pkg/FR-2000-01-12/pdf/00-3.pdf#page=50**.
30 B. R. Stern, *J. Toxicol. Environ. Health, Part A*, 2010, **73**, 114.
31 H. S. Jung, P. S. Kwon, J. W. Lee, J. I. Kim, C. S. Hong, J. W. Kim and J. S. Kim, *J. Am. Chem. Soc.*, 2009, **131**, 2008.
32 K. J. Barnham, C. L. Masters and A. I. Bush, *Nat. Rev. Drug Discovery*, 2004, **3**, 205.
33 G. Zhou, Y. Cheng, L. Wang, X. Jing and F. Wang, *Macromolecules*, 2005, **38**, 2148.
34 Y. Zhang, C. B. Murphy and W. E. Jones, *Macromolecules*, 2002, **35**, 630.

35 B. Zambelli, F. Musiani, S. Benini and S. Ciurli, *Acc. Chem. Res.*, 2011, **44**, 520.
36 S. W. Ragsdale, *J. Biol. Chem.*, 2009, **284**, 18571.
37 A. Sigel, H. Sigel and R. K. Sigel, *Nickel and Its Surprising Impact in Nature*, John Wiley & Sons, 2007, p. 728.
38 S. C. Dodani, Q. He and C. J. Chang, *J. Am. Chem. Soc.*, 2009, **131**, 18020.
39 Z. Kowser, U. Rayhan, T. Akther, C. Redshaw and T. Yamato, *Mater. Chem. Front.*, 2021, **5**, 2173.
40 B. Daly, J. Ling and A. P. De Silva, *Chem. Soc. Rev.*, 2015, **44**, 4203.
41 C. Kar, M. D. Adhikari, A. Ramesh and G. Das, *Inorg. Chem.*, 2013, **52**, 743.
42 N. P. Junager, J. Kongsted and K. Astakhova, *Sensors*, 2016, **16**, 1173.
43 R. Pandey, A. Kumar, Q. Xu and D. S. Pandey, *Dalton Trans.*, 2020, **49**, 542.
44 F. V. Englich, T. C. Foo, A. C. Richardson, H. Ebendorff-Heidepriem, C. J. Sumby and T. M. Monro, *Sensors*, 2011, **11**, 9560.
45 P. Torawane, K. Tayade, S. Bothra, S. K. Sahoo, N. Singh, A. Borse and A. Kuwar, *Sens. Actuators, B*, 2016, **222**, 562.
46 T. M. Asha, E. Shiju, C. Keloth and M. R. P. Kurup, *Appl. Organomet. Chem.*, 2020, **34**, e5520.
47 K. Poongodi, P. Saravana Kumar, R. Shanmugapriya, C. Nandhini and K. P. Elango, *Spectrochim. Acta, Part A*, 2021, **249**, 119288.
48 D. Y. Patil, N. B. Khadke, A. A. Patil and A. V. Borhade, *Results Chem.*, 2022, **4**, 100658.
49 S. Santhi and K. Abinaya, *Indian Pat. Appl.*, 2022, 29.
50 E. T. Aljohani, M. R. Shehata, F. Alkhatib, S. O. Alzahrani and A. M. Abu-Dief, *Appl. Organomet. Chem.*, 2021, **35**, e6154.
51 E. T. Aljohani, M. R. Shehata and A. M. Abu-Dief, *Appl. Organomet. Chem.*, 2021, **35**, e6169.
52 H. M. A. El-Lateef, T. El-Dabea, M. M. Khalaf and A. M. Abu-Dief, *Int. J. Mol. Sci.*, 2022, **23**, 6418.
53 F. S. Aljohani, O. A. Omran, E. A. Ahmed, E. S. Al-Farraj, E. F. Elkady, A. Alharbi, N. M. El-Metwaly, I. O. Barnawi and A. M. Abu-Dief, *Inorg. Chem. Commun.*, 2023, **148**, 110331.
54 Z. Shamsollahi and A. Partovinia, *J. Environ. Manage.*, 2019, **246**, 314.
55 S. J. Cobbina, A. B. Duwiejuah, R. Quansah, S. Obiri and N. Bakobie, *Int. J. Environ. Res. Public Health*, 2015, **12**, 10620.
56 K. Shakeela, A. S. Dithya, C. J. Rao and G. R. Rao, *J. Chem. Sci.*, 2015, **127**, 133.
57 M. Kuate, M. A. Conde, E. Ngandung Mainsah, A. G. Paboudam, F. M. M. Tchieno, K. I. Ketchemen and P. T. Ndifon, *J. Chem.*, 2020, **2020**, 5238501.
58 V. S. Vasantha and V. S. Muralidharan, *Proc. Natl. Acad. Sci. U. S. A.*, 1994, **106**, 825.
59 R. Sekar, S. Jayakrishnan and V. S. Muralidharan, *Trans. Inst. Met. Finish.*, 2005, **83**, 300.
60 E. T. Shamkhy, *J. Al-NahrainUniv. Sci.*, 2015, **18**, 39.
61 A. P. Gulya, V. I. Tsapkov, D. Poirier, K. Aruksandei and E. Pakhontsu, *Russ. J. Gen. Chem.*, 2010, **80**, 1351.
62 T. Tunç, M. Sarı, M. Sadıkoğlu and O. Büyükgüngör, *J. Chem. Crystallogr.*, 2009, **39**, 672.
63 Y. Huang, C. Rong, R. Zhang and S. Liu, *J. Mol. Model.*, 2017, **23**, 3.
64 J. Yu, N. Q. Su and W. Yang, *J. Am. Chem. Soc.*, 2022, **2**, 1383.
65 M. U. Khan, M. Khalid, I. Shafiq, R. A. Khera, Z. Shafiq, R. Jawaria, M. Shafiq, M. M. Alam, A. A. C. Braga, M. Imran, F. Kanwal, Z. Xu and C. Lu, *J. Saudi Chem. Soc.*, 2021, **25**, 101339.
66 J. L. Gázquez, A. Cedillo and A. Vela, *J. Phys. Chem. A*, 2007, **111**, 1966.
67 P. K. Chattaraj, A. Chakraborty and S. Giri, *J. Phys. Chem. A*, 2009, **113**, 10068.
68 J. J. Philips, M. A. Hudspeth, P. M. Browne and J. E. Peralta, *Chem. Phys. Lett.*, 2010, **495**, 146.
69 A. D. Becke, *Phys. Rev. A: At., Mol., Opt. Phys.*, 1988, **38**, 3098.
70 M. J. Frisch, *et al.*, *Gaussian 09, Revision D.01*, 2009.
71 R. Ditchfield, W. J. Hehre and J. A. Pople, *J. Chem. Phys.*, 1971, **54**, 724.
72 P. Y. Hay and W. R. Wadt, *J. Chem. Phys.*, 1985, **82**, 299.
73 R. Dennington, T. Keith and J. Millam, *GaussView, Version 5*, Shawnee Mission, KS Semichem Inc., 2009.
74 C. Legault, CYLview.
75 R. G. Pearson, *Proc. Natl. Acad. Sci. U. S. A.*, 1986, **83**, 8440.
76 R. G. Pearson, *J. Chem. Educ.*, 1987, **64**, 561.
77 J. L. Reed, *J. Phys. Chem. A*, 1997, **101**, 7396.
78 R. G. Parr, L. V. Szentpály and S. Liu, *J. Am. Chem. Soc.*, 1999, **121**, 1922.